



**Macroscopic and microscopic description of phase transition in cerium isotopes**P. Alexa <sup>\*</sup>*Department of Physics, VŠB – Technical University Ostrava, 17. listopadu 2172/15, CZ-708 00 Ostrava, Czech Republic*

M. Abolghasem

*Department of Physics and IT4 Innovations, VŠB – Technical University Ostrava, 17. listopadu 2172/15, CZ-708 00 Ostrava, Czech Republic*

G. Thiamova

*Universite Grenoble 1, CNRS, LPSC, Institut Polytechnique de Grenoble, IN2P3, F-38026 Grenoble, France*D. Bonatsos *Institute of Nuclear and Particle Physics, N.C.S.R. Demokritos, GR-15310 Aghia Paraskevi, Attiki, Greece*T. R. Rodríguez <sup>†</sup>*Departamento de Física Teórica and Centro de Investigación Avanzada en Física Fundamental-CIAFF, Universidad Autónoma de Madrid, E-28049, Madrid, Spain*P.-G. Reinhard *Institute for Theoretical Physics II, University of Erlangen, Staudstr. 7, D-91058 Erlangen, Germany*

(Received 20 January 2022; accepted 6 October 2022; published 2 November 2022)

The spherical-to-deformed phase transition in cerium isotopes recently suggested to occur between  $^{146}\text{Ce}$  and  $^{148}\text{Ce}$  has been examined in the framework of the macroscopic algebraic collective model and two microscopic approaches, namely Skyrme-Hartree-Fock + Bardeen-Cooper-Schrieffer (BCS) calculations and the symmetry conserving configuration mixing method with Gogny energy density functionals applied also to the neighboring nuclei along the cerium isotopic chain. Possible spectral signatures of the phase transition are discussed in more details. The microscopic calculations predict octupole softness manifested by rather flat potential energy curves as a function of the octupole deformation parameter  $\beta_3$  for  $^{146}\text{Ce}$  and  $^{148}\text{Ce}$  and shape coexistence characterized by axially symmetric  $0^+$  states, triaxial  $2^+$  bands, and octupole deformation for the lowest  $1^-$  states.

DOI: [10.1103/PhysRevC.106.054304](https://doi.org/10.1103/PhysRevC.106.054304)**I. INTRODUCTION**

Investigations of the first order quantum shape phase transitions from spherical to prolate axially deformed nuclei initiated by the seminal paper of Iachello [1] introducing the concept of the  $X(5)$  critical-point symmetry have been the subject of research for almost two decades [2–5]. Especially in the region of even-even Ce, Nd, Sm, Dy, and Gd isotopes, several candidates for  $X(5)$  nuclei have been proposed (cf., e.g., [6–11]). The Nd, Sm, and Gd with  $N = 90$ , which are known to be good examples of  $X(5)$ , have been considered using relativistic energy-density functionals restricted to axially symmetric shapes in [12]. On the other hand, Xe and Ba isotopes with  $A \geq 130$ , expected to be close to the  $E(5)$  critical point symmetry, have been considered using relativistic energy-density functional allowing triaxial shapes in [13].

Recently, the shape phase transition in cerium isotopes around  $N = 88$ – $90$  has been studied both experimentally and theoretically in Refs. [14,15]. The fast electronic timing method enabled to measure the lifetime of the  $4_1^+$  state for the first time and to extract the  $B_{4/2} = B(E2; 4_1^+ \rightarrow 2_1^+)/B(E2; 2_1^+ \rightarrow 0_1^+)$  value of 1.52(12) close to the  $X(5)$  prediction of 1.58. Based on a careful IBM-1 analysis of the available experimental data they concluded that the spherical-to-deformed phase transition in cerium isotopes happens between  $^{146}\text{Ce}$  and  $^{148}\text{Ce}$ , and  $^{148}\text{Ce}$  can be better described within the  $X(5) - \beta^8$  model. They also pointed out an increasing role of the  $\gamma$  degree of freedom in these nuclei. These conclusions were supported by the microscopic analysis in the framework of the five-dimensional quadrupole collective Hamiltonian (5DQCH) [16].

In this paper we extend the analysis of the phase transition in cerium isotopes performed in Ref. [14]. First in Sec. II we reexamine possible spectral signatures of the  $X(5)$  phase transition in more details. In Sec. III we analyze the cerium isotopes within the algebraic collective model (ACM) and show that it is capable to remove the freedom in the  $\gamma$  band

<sup>\*</sup>petr.alex@vsb.cz<sup>†</sup>tr.rodriguez@ucm.es

position in relation to the ground and  $\beta$  bands inherent in pure  $X(5)$  model [2]. In Secs. IV and V we turn to microscopic description of the chain of cerium isotopes using Skyrme-Hartree-Fock + Bardeen-Cooper-Schrieffer (BCS) calculations further processed in the generator coordinate method at the level of the Gaussian overlap approximation [17] and the symmetry conserving configuration mixing method with Gogny energy density functionals [18].

## II. SYSTEMATIC STUDY OF THE PHASE TRANSITION REGION AROUND $N = 90$

In the literature one can find two types of experimental fingerprints of the phase transition between the spherical vibrator  $U(5)$  and deformed axially symmetric rotor  $SU(3)$  via the  $X(5)$  critical point: (a) energy ratios and (b)  $B(E2)$  reduced-probability ratios.

In this section we focus only on the energy ratios. The fingerprints based on  $B(E2)$  values are often difficult to measure because of their substantial experimental uncertainties and only a slight variation as a function of the nuclear structure.

Besides the frequently used ratio  $R_{42} = E(4_1^+)/E(2_1^+)$  that equals 2.9 in the  $X(5)$  limit one can also investigate other ratios, namely  $R_{022} = E(0_2^+)/E(2_1^+)$  that equals 5.67 in the  $X(5)$  limit,  $R_{422} = E(4_2^+)/E(2_2^+)$  that equals 1.43 in the  $X(5)$  limit,  $R_{222} = E(2_{2,\beta}^+)/E(2_1^+)$  that equals 7.48 in the  $X(5)$  limit [ $E(2_{2,\beta}^+)$  represents the second excited  $2^+$  state or the  $2^+$  member of the  $\beta$  band], and  $R_{60} = E(6_1^+)/E(0_2^+)$  that equals 0.96, i.e., approximately 1 in the  $X(5)$  limit [19]. In addition, we will also investigate the ratio  $R_{232} = E(2_{3,\gamma}^+)/E(2_1^+)$  that is not constrained in pure  $X(5)$  because the harmonic oscillator parameters in  $\gamma$  direction are not fixed in this limit [2] [ $E(2_{3,\gamma}^+)$  represents the third excited  $2^+$  state or the  $2^+$  band head of the  $\gamma$  band].

The energy ratios for the region of interest for the chains of Ce, Nd, Sm, Gd, and Dy isotopes are presented in Fig. 1. The degree of collectivity in each isotopic chain increases with increasing neutron number and undergoes the phase transition around  $N = 90$ . One can see that for  $N = 90$  the ratios  $R_{42}$ ,  $R_{022}$ ,  $R_{222}$ , and  $R_{60}$  are quite close for all chains and also close to the  $X(5)$  value. The ratio  $R_{422}$  for all chains, on the other hand, departs from the  $X(5)$  value [the anomalous value for  $^{144}\text{Ce}$  ( $N = 86$ ) corresponds to a  $\gamma$ -like band and not to a  $\beta$ -like band as the other values], and the ratio  $R_{232}$  equals approximately 8 for  $^{150}\text{Nd}$ ,  $^{152}\text{Sm}$ , and  $^{154}\text{Gd}$ , whereas for  $^{148}\text{Ce}$  and  $^{156}\text{Dy}$  it is around 6. One can also notice only a modest increase of  $R_{232}$ ,  $R_{022}$  and  $R_{222}$  for the cerium isotopes when approaching  $N = 90$  compared to a rather steep change for the other isotopes. This may indicate that the cerium isotopes do not represent a pure example of the  $X(5)$  phase transition.

## III. ALGEBRAIC COLLECTIVE MODEL

The ACM, introduced as a computationally tractable version of the Bohr model (BM) [20] restricted to rotational and quadrupole vibrational degrees of freedom, is characterized by a well defined algebraic structure. Unlike the conventional  $U(5) \supset SO(5) \supset SO(3)$  dynamical subgroup chain used, for example, by the Frankfurt group [21,22], the ACM makes use

of the subgroup chain

$$SU(1, 1) \times SO(5) \supset U(1) \times SO(3) \supset SO(2) \quad (1)$$

to define basis wave functions as products of  $\beta$  wave functions and  $SO(5)$  spherical harmonics. Several advantages result from this choice of dynamical subgroup chain: (i) matrix elements of BM operators can be calculated analytically; (ii) collective model calculations converge an order of magnitude more rapidly for deformed nuclei than in the  $U(5) \supset SO(5)$  bases. Thus, the ACM combines the advantages of the BM and the IBM and makes collective model calculations a simple routine procedure [23–26]. A detailed description of the ACM can be found in Ref. [23].

The most general ACM Hamiltonian can be written in the form [27]

$$\begin{aligned} \hat{H} = & \frac{-\nabla^2}{2M} + a_1 + a_2\beta^2 + a_3\beta^4 + \frac{a_4}{\beta^2} + a_5\beta \cos 3\gamma \\ & + a_6\beta^3 \cos 3\gamma + a_7\beta^5 \cos 3\gamma + \frac{a_8}{\beta} \cos 3\gamma + a_9 \cos^2 3\gamma \\ & + a_{10}\beta^2 \cos^2 3\gamma + a_{11}\beta^4 \cos^2 3\gamma + \frac{a_{12}}{\beta^2} \cos^2 3\gamma \\ & + \frac{a_{13}}{\hbar^2} [\hat{\pi} \otimes \hat{q} \otimes \hat{\pi}]_0, \end{aligned} \quad (2)$$

where

$$\nabla^2 = \frac{1}{\beta^4} \frac{\partial}{\partial \beta} \beta^4 \frac{\partial}{\partial \beta} + \frac{1}{\beta^2} \hat{\Lambda} \quad (3)$$

is the Laplacian in the five-dimensional collective model space and  $\hat{\Lambda}$  is the  $SO(5)$  angular momentum operator [28]. Such a Hamiltonian, expressed in terms of the quadrupole deformation parameters  $\beta$  and  $\gamma$  serves as a useful starting point for a description of a wide range of nuclear collective spectra.

While a simplified form

$$\begin{aligned} \hat{H}(M, \alpha, \kappa, \chi) = & \frac{-\nabla^2}{2M} + \frac{1}{2}M[(1 - 2\alpha)\beta^2 + \alpha\beta^4] \\ & - \chi\beta \cos 3\gamma + \kappa \cos^2 3\gamma, \end{aligned} \quad (4)$$

can be used to study the second order phase transition from  $U(5)$  to  $O(6)$  via an  $E(5)$  critical point [29–31], an approximation of the  $X(5)$  limit can be obtained for the ACM Hamiltonian

$$\begin{aligned} \hat{H}(M, \alpha, \kappa, \chi) = & \frac{-\nabla^2}{2M} + \frac{1}{2}M[(1 - 2\alpha)\beta^2 + \alpha\beta^4] \\ & - \chi\beta^3 \cos 3\gamma + \kappa \cos^2 3\gamma. \end{aligned} \quad (5)$$

The last term in the Hamiltonian (4), proportional to  $\cos^2 3\gamma$ , can induce a triaxial minimum of the potential. A delicate competition between all the terms in the potential and the last two terms in particular will determine whether the potential energy minimum will remain axially symmetric (the term proportional to  $\cos 3\gamma$  dominates) or will be driven to a triaxial minimum by the last term.

In the case of the phase transition from a spherical vibrator  $U(5)$  to the axially symmetric rotor  $SU(3)$  we can set  $\kappa = 0$

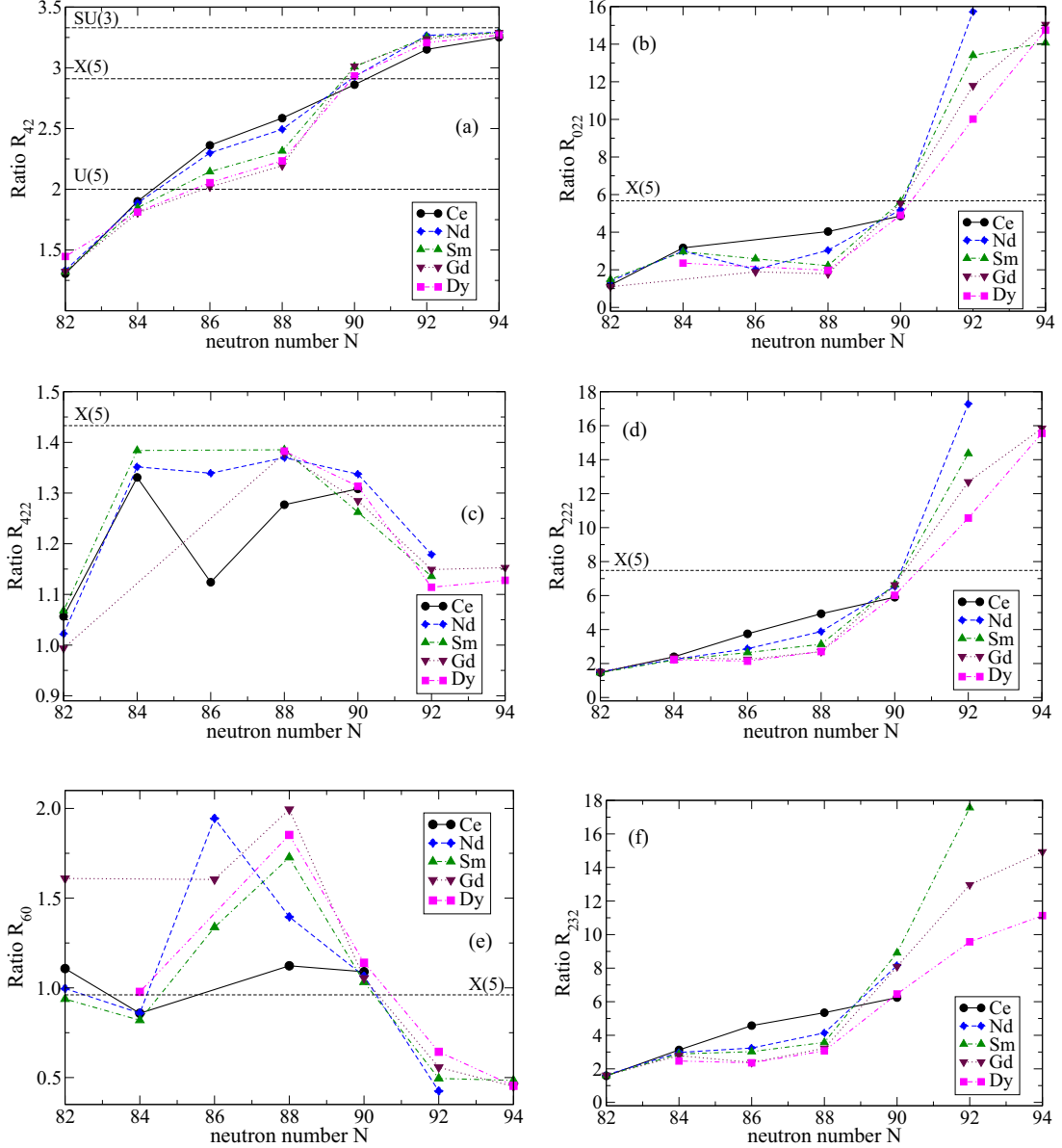


FIG. 1. Experimental energy ratios  $R_{42}$  (a),  $R_{022}$  (b),  $R_{422}$  (c),  $R_{222}$  (d),  $R_{60}$  (e), and  $R_{232}$  (f) for Ce, Nd, Sm, Gd, and Dy isotopes. For more details see the text.

and  $\cos 3\gamma = 1$ . The ACM potential then reads

$$V = \frac{1}{2}M[(1 - 2\alpha)\beta^2 + \alpha\beta^4] - \chi\beta^3. \quad (6)$$

To identify its shape the first and second derivatives of  $V$  have to be calculated:

$$\begin{aligned} dV/d\beta &= M(1 - 2\alpha)\beta + 2M\alpha\beta^3 - 3\chi\beta^2, \\ d^2V/d\beta^2 &= M(1 - 2\alpha) + 6M\alpha\beta^2 - 6\chi\beta. \end{aligned} \quad (7)$$

From the cubic equation  $dV/d\beta = 0$ , i.e.,  $\beta^3 + (1/2\alpha - 1)\beta - 3\chi\beta^2/2M\alpha = 0$ , we get extremes of the potential  $V$ . There is always an extreme for  $\beta = 0$  that corresponds to a minimum for  $\alpha < 0.5$  and a maximum for  $\alpha > 0.5$ . For  $\alpha$  slightly lower than 0.5 we get another prolate minimum while for  $\alpha > 0.5$  we always get two minima, one for  $\beta > 0$  (prolate) and one for  $\beta < 0$  (oblate). They are symmetric for

$\chi/M \rightarrow 0$  and asymmetric for higher values of  $\chi/M$ , where we get a weaker oblate one and a deeper prolate one (see Fig. 2), a similar picture to that obtained in Sec. V for the potential energy curves (PEC) as a function of quadrupole deformation  $\beta_2$  using the microscopic Skyrme-HF + BCS approach. We can therefore conclude that a phase transition in this version of ACM occurs in the vicinity of  $\alpha = 0.5$ . In the next section we will apply the ACM to  $^{146}\text{Ce}$  and  $^{148}\text{Ce}$ .

#### IV. NUMERICAL RESULTS OBTAINED WITHIN THE ACM

In the ACM calculations, we fitted the model parameters,  $M$ ,  $\alpha$ , and  $\chi$ , to the experimentally known low-lying states in  $^{146}\text{Ce}$  and  $^{148}\text{Ce}$ . Both theoretical and model spectra are shown in Fig. 3 and compared to that of the  $X(5)$  limit. We observe

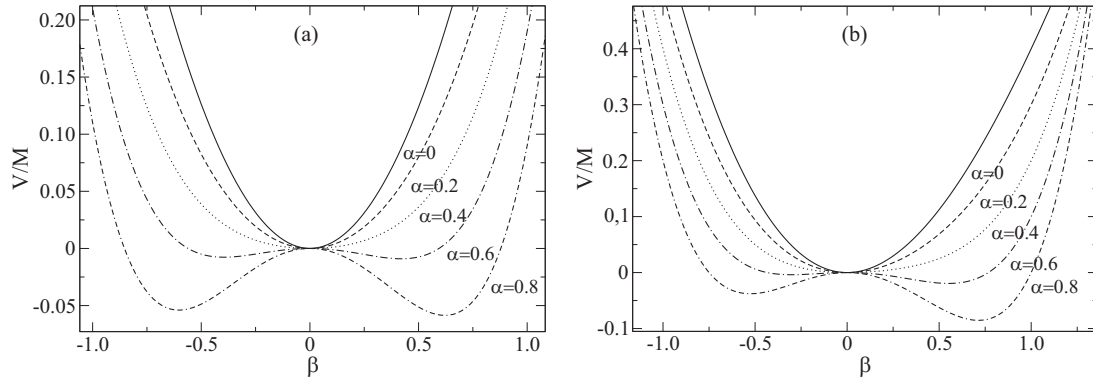


FIG. 2. ACM potential as a function of  $\beta$  for different values of  $\alpha$  and a small value of  $\chi/M = 0.01$  (a) and for a higher value of  $\chi/M = 0.1$  (b).

only a moderate change of the model parameters when moving from  $^{146}\text{Ce}$  to  $^{148}\text{Ce}$  ( $M = 45 \rightarrow 50$ ,  $\alpha = 0.60 \rightarrow 0.62$ ,  $\chi = 5.8 \rightarrow 6.1$ ). It should be also noted that the position of the lowest  $2^+$   $\gamma$  band not defined in the  $X(5)$  model is fixed in the ACM by the chosen parameters  $M$ ,  $\alpha$ , and  $\chi$ .

For  $^{146}\text{Ce}$  the ground state and the  $\beta$ -like bands are well reproduced while the next experimental  $0^+$  band head and the lowest  $2^+$  band head lie slightly lower than the prediction of ACM. It is clear that in this nucleus the  $0_3^+$  state lies substantially lower than one would expect in the  $X(5)$  limit and the moments of inertia of the ground state and the  $\beta$ -like bands are higher than in the  $X(5)$  limit (Fig. 3).

ACM predicts  $B_{4/2} = 1.80$  and different ratio  $B(E2, 2_2^+ \rightarrow 2_1^+)/B(E2, 0_2^+ \rightarrow 2_1^+) = 0.40$  compared to 0.13 in the  $X(5)$  limit. Unfortunately, in this nucleus only the experimental value of the  $B(E2, 2_1^+ \rightarrow 0_1^+)$  transition is known. Therefore, we cannot compare our ACM calculations with the experimental data on  $E2$  transitions.

For  $^{148}\text{Ce}$  the experimental spectrum (Fig. 3) contains a lot of characteristics typical for the  $X(5)$  limit. The experimental moment of inertia of the ground-state band is slightly lower than the ACM value and higher than the  $X(5)$  prediction while the experimental value for the  $0^+$   $\beta$ -like band is slightly higher than those predicted by the ACM and the  $X(5)$  limit. The ACM also predicts the lowest  $2^+$   $\gamma$  band head at a higher energy than is experimentally observed.

The ACM gives  $B_{4/2} = 1.50$  in agreement with the experimental value of 1.52(12) and slightly lower than the  $X(5)$  value of 1.58. It predicts considerably different ratio  $B(E2, 2_2^+ \rightarrow 2_1^+)/B(E2, 0_2^+ \rightarrow 2_1^+) = 0.66$  compared to 0.13 in the  $X(5)$  limit. Unfortunately, this prediction cannot be verified by the experimental data.

It is necessary to turn to microscopic studies of the structure of these nuclei to ascertain the degree of collectivity on more fundamental grounds along the chain of the investigated cerium isotopes. First we investigate ground-state deformations in the framework of the constrained Skyrme-Hartree-Fock model, then we focus on the structure of the ground state and low-lying states within the framework of the symmetry conserving configuration mixing method with Gogny energy density functionals.

### V. SKYRME HARTREE-FOCK CALCULATIONS

Among self-consistent mean-field methods the Skyrme-Hartree-Fock model (SHF) is the most widely used [33] and represents another possibility to investigate nuclear ground state (g.s.) properties. There are plenty of SHF functional parametrizations available in the literature. We refer here to a recent family of parametrizations which was derived from least-square fitting of its free parameters to a large pool of selected g.s. observables and, optionally, other nuclear properties [34]. This family includes an optimization to ground

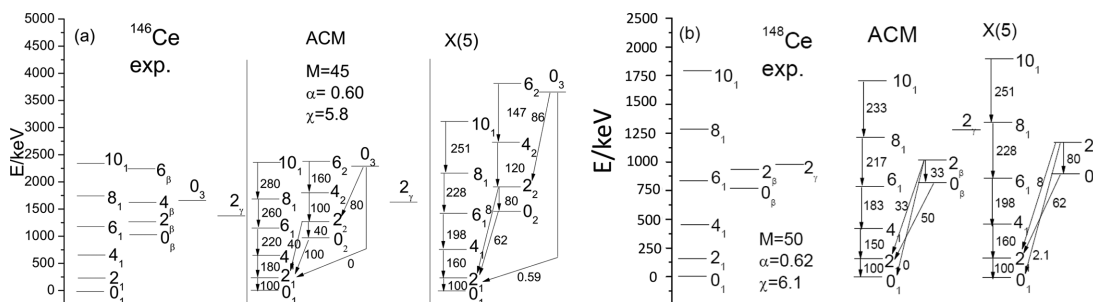


FIG. 3. Experimental spectrum of  $^{146}\text{Ce}$  [32] and its ACM counterpart (a). The same for  $^{148}\text{Ce}$  (b). Both spectra are compared to the expected spectrum at the  $X(5)$  limit. The energy difference of the  $2_1^+$  and  $0_1^+$   $X(5)$  states is fitted to the experimental value in  $^{146}\text{Ce}$  and  $^{148}\text{Ce}$ , respectively.

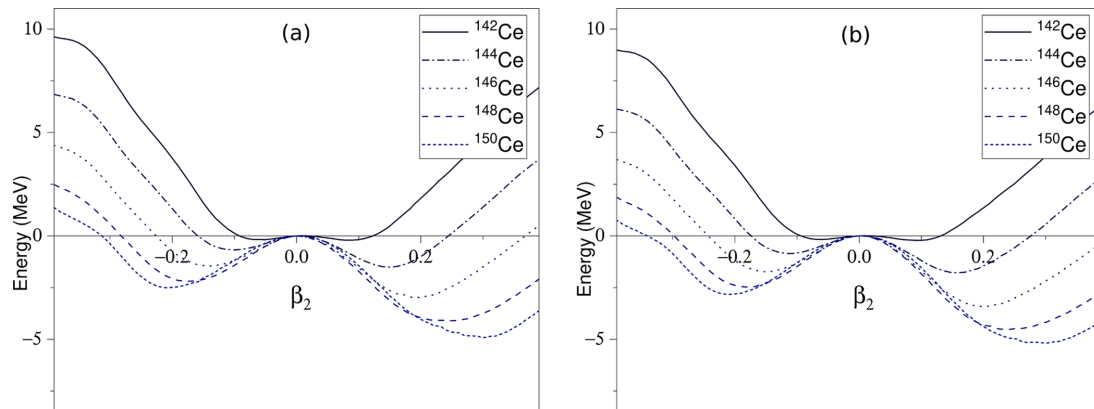


FIG. 4. PEC as a function of  $\beta_2$  for the cerium isotopes for two SHF parametrizations, SV-bas (a) and SV-tls (b).

state properties only, denoted SV-min, and a couple of related parameterizations with dedicated variation of nuclear matter properties (incompressibility, symmetry energy, effective isoscalar and isovector mass) [34]. We have checked for the present test cases all of them and in addition three older choices, namely Sk-M\*, SLy6, and SkI3. For presentation we confine here to SV-tls best fitting the binding energies of the studied cerium isotopes [35], and to SV-bas as base point for dedicated variation of nuclear matter properties. In calculations using the axial SHF code SKYAX with a density-dependent  $\delta$ -force interaction in the pairing channel [36] single-particle levels up to 75 MeV were taken into account (eight oscillator shells). We also checked the possible triaxiality using the code SKY3D [37]. Triaxiality was observed only for  $N < 82$  that justifies our approach that the investigated nuclei can be analyzed using the axial SHF code SKYAX.

In the  $X(5)$  limit one would expect to observe a typical bump structure in the potential energy curve (PEC) calculations as a function of the quadrupole deformation parameter  $\beta_2$  [38].

Phase transitions along the chain of cerium isotopes are illustrated in Figs. 4–6 for the two chosen parametrizations and quadrupole  $\beta_2$ , octupole  $\beta_3$ , and hexadecapole  $\beta_4$  deformations. It is clearly seen that for both parametrizations we observe two asymmetric minima in the  $\beta_2$  PEC, a weaker oblate one and a deeper prolate one. Both minima become deeper along the investigated chain of cerium isotopes and

the absolute values  $|\beta_2|$  for oblate and prolate minima increase. The resulting PECs for octupole deformation  $\beta_3$  are Skyrme-parametrization dependent: For SV-bas the highest octupole deformation is observed for  $^{146}\text{Ce}$  and for  $^{144}\text{Ce}$  and  $^{148}\text{Ce}$  the PECs are quite flat in  $\beta_3$ , thus resembling a phase transition critical point that can be approximated by an infinite square well in  $\beta_3$  whereas for SV-tls no well-pronounced octupole minima are observed. To see the evolution of both quadrupole and octupole deformations along the cerium isotopic chain more clearly, the potential energy surfaces (PES) along the  $\beta_2$ - $\beta_3$  plane are shown for the parametrization SV-bas in Fig. 7. For other Skyrme parametrizations one gets a qualitatively similar picture demonstrating that PES are dominated by shell structure and this is a topological property, not so sensitive to details of the force. Hexadecapole deformation  $\beta_4$  practically does not depend on the parametrization and is positive and increasing with increasing  $A$ .

To find the energies of the lowest states in  $^{148}\text{Ce}$  the results of the quadrupole-constrained calculations for the SV-bas SHF parametrization were further processed in the generator coordinate method (GCM) at the level of the Gaussian overlap approximation [17] neglecting octupole deformation. The nucleus was found to be still considerably soft having a large collective correlation energy of 3 MeV. The lowest collective state  $2_1^+$  is predicted at 0.135 MeV which is close to the experimental value of 0.158 MeV. The other positive parity

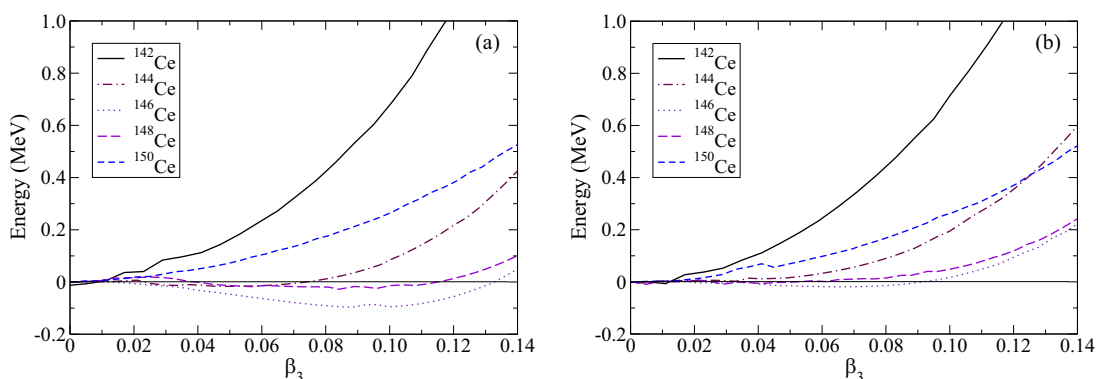


FIG. 5. PEC as a function of  $\beta_3$  for the cerium isotopes for two SHF parametrizations, SV-bas (a) and SV-tls (b).

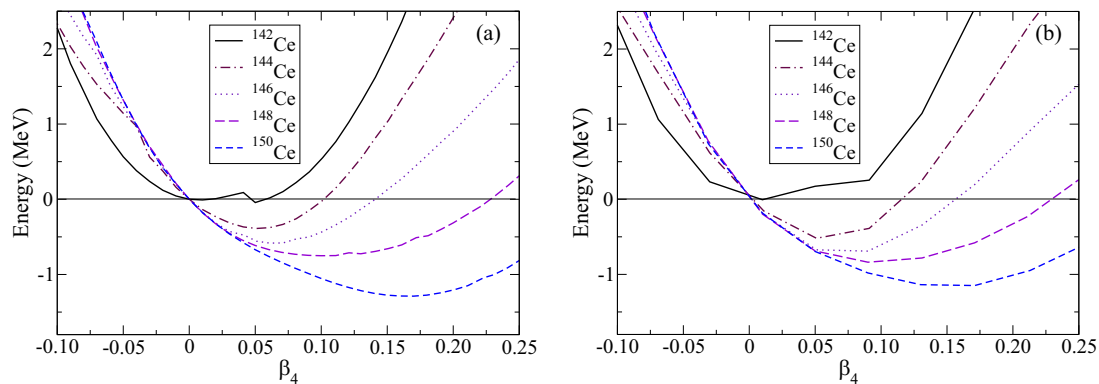


FIG. 6. PEC as a function of  $\beta_4$  for the cerium isotopes for two SHF parametrizations, SV-bas (a) and SV-tls (b).

low-spin excited states predicted are (experimental values in parentheses):  $4_1^+$  at 0.563 MeV (0.453 MeV),  $0_2^+$  at 0.90 MeV (0.77 MeV),  $2_2^+$  at 1.14 MeV (0.94 MeV), and  $2_3^+$  at 1.22 MeV (0.99 MeV).

Unfortunately, we cannot investigate negative parity states in our approach, because our GCM code is restricted to a reflection-symmetric mean field. Therefore, we turn to the most microscopic approach in our study, the symmetry conserving configuration mixing calculations that enable us to investigate also octupole deformation and negative parity states.

## VI. SYMMETRY CONSERVING CONFIGURATION MIXING CALCULATIONS

The last method used to study the structure of Ce isotopes around  $N = 90$  is based on two Gogny D1S energy density functionals (EDF) that include beyond-mean-field effects within the symmetry conserving configuration mixing (SCCM) framework. Here, the nuclear wave functions are obtained by mixing symmetry-restored intrinsic HFB states defined along collective degrees of freedom. The coefficients of the linear combination of such symmetry-restored states are obtained within the generator coordinate method (GCM). The two implementations used in this work differ in a) the collective coordinates explored, b) the symmetries that are restored, and c) the way the intrinsic HFB states are found. In the first approach, dubbed as  $\text{SCCM}_{(\beta_2, \beta_3)}$ , axial quadrupole ( $\beta_2$ ) and octupole ( $\beta_3$ ) degrees of freedom are taken into account by building a set of intrinsic wave functions,  $\{|\phi(\beta_2, \beta_3)\rangle\}$ , that are obtained by the minimization of the HFB energy with constraints in such collective coordinates. Then, these HFB states are subsequently projected onto good parity (positive and negative), number of particles and (axial) angular momentum, and, finally, mixed following the GCM method (see Ref. [39]). The second approach,  $\text{SCCM}_{(\beta_2, \gamma)}$ , considers quadrupole deformations (axial and nonaxial) without breaking the parity symmetry. In this case, a more involved variation after particle number projection method (VAPNP), where the particle number projected energy with constraints is minimized, is used to build the set intrinsic HFB wave functions. Then, the symmetry restoration involves particle number and triaxial angular momentum projection. These

projected states are finally mixed to build the nuclear states (see Ref. [18]). The main differences between the two Gogny EDFs are 1) the superiority of VAPNP to HFB to take into account pairing correlations; 2) triaxial quadrupole shapes allow the study of positive parity states with an odd value of the angular momentum (e.g., triaxial bands,  $\gamma$  bands, etc.); and, 3) axial octupole shapes allow the study of negative parity bands with an odd value of the angular momentum. Unfortunately, the inclusion of triaxial and octupole shapes on the same footing within Gogny-SCCM methods is still out of the present computational capabilities.

As shown in the previous section, the first step in the description of the collectivity of a given nucleus is the analysis of the PECs. In the top panel of Fig. 8 we represent the HFB energy in the  $(\beta_2, \beta_3)$  plane for the  $^{146-150}\text{Ce}$  isotopes. First, we observe that the energy is symmetric about  $\beta_3 = 0$  because the nuclear interaction is parity symmetric. Additionally, the HFB ground state energy is found at quadrupole prolate deformations around  $\beta_2 \approx 0.3$  and a secondary minimum at quadrupole oblate deformations  $\beta_2 \approx -0.2$ . More interestingly, the absolute minimum of the surface is obtained at a nonzero value of  $\beta_3 \approx 0.1$  in the isotope  $^{146}\text{Ce}$ , while the surface is rather flat around the minimum along  $\beta_3$  for  $^{148}\text{Ce}$  and, finally, more rigid in the nucleus  $^{150}\text{Ce}$ . These results anticipate the relevance of octupole configurations in this region, especially in the isotope  $^{146}\text{Ce}$ , and are consistent with the Skyrme calculations shown above.

Concerning the triaxial degree of freedom, we plot in the bottom panel of Fig. 8 the VAPNP energy in the  $(\beta_2, \gamma)$  plane for the  $^{146-150}\text{Ce}$  isotopes. Here, we observe that the absolute minimum in the three isotopes are found in prolate axial symmetric states ( $\gamma = 0^\circ$ ) at slightly smaller values of  $\beta_2$  than those obtained with mean-field (HFB) calculations. This small difference could be attributed to the larger pairing correlations obtained with the VAPNP method that make the system less deformed. Nevertheless, the energy surfaces around the prolate minimum are rather stiff and we do not expect a large effect of the triaxiality in the ground state bands of these nuclei. Moreover, the oblate minimum found in the axial calculation is a saddle-point in the triaxial calculation. Finally, it is important to note that none of these energy surfaces show clear signatures of the  $X(5)$  symmetry.

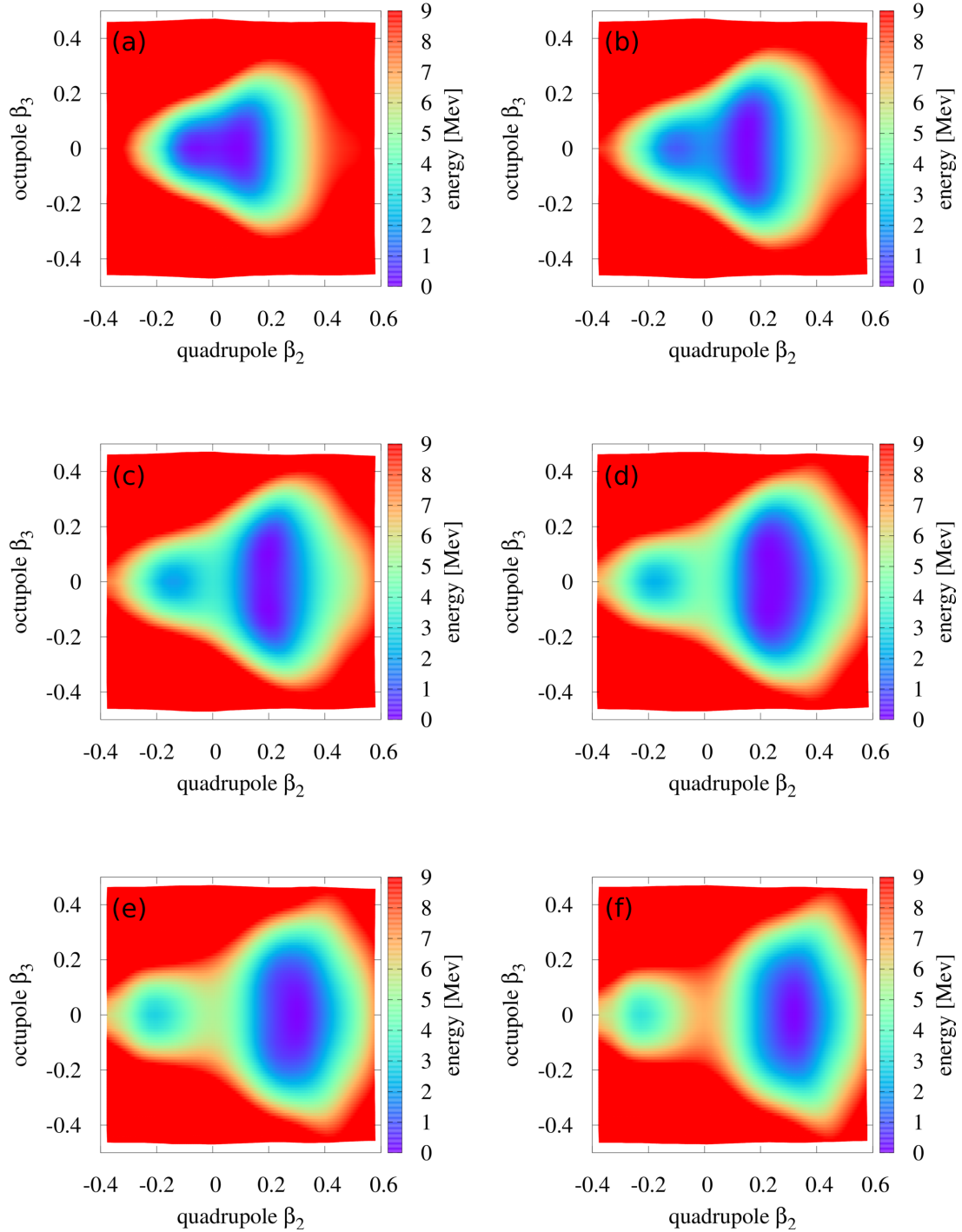


FIG. 7. SHF + BCS potential energy surfaces along the axial  $\beta_2$ - $\beta_3$  plane for (a)  $^{142}\text{Ce}$ , (b)  $^{144}\text{Ce}$ , (c)  $^{146}\text{Ce}$ , (d)  $^{148}\text{Ce}$ , (e)  $^{150}\text{Ce}$ , and (f)  $^{152}\text{Ce}$ .

The final results are obtained within the SCCM formalism after solving the GCM equations with symmetry-projected wave functions that provides the ground-state and excitation energies, and the collective wave functions (c.w.f.) [40]. The latter represent the weights of the different intrinsic deformations in each nuclear wave function.

Concerning the  $\text{SCCM}_{(\beta_2, \beta_3)}$  results, we obtain a positive parity ground state band ( $0_1^+$ ,  $2_1^+$ ,  $4_1^+$ , etc.) and a negative parity band associated to it ( $1_1^-$ ,  $3_1^-$ ,  $5_1^-$ , etc.) in the three  $^{146-150}\text{Ce}$  isotopes. The c.w.f.'s of the band heads are shown in Fig. 9 where we clearly see that the three isotopes are quadrupole deformed and, for  $^{146-148}\text{Ce}$  isotopes, an octupole deformation

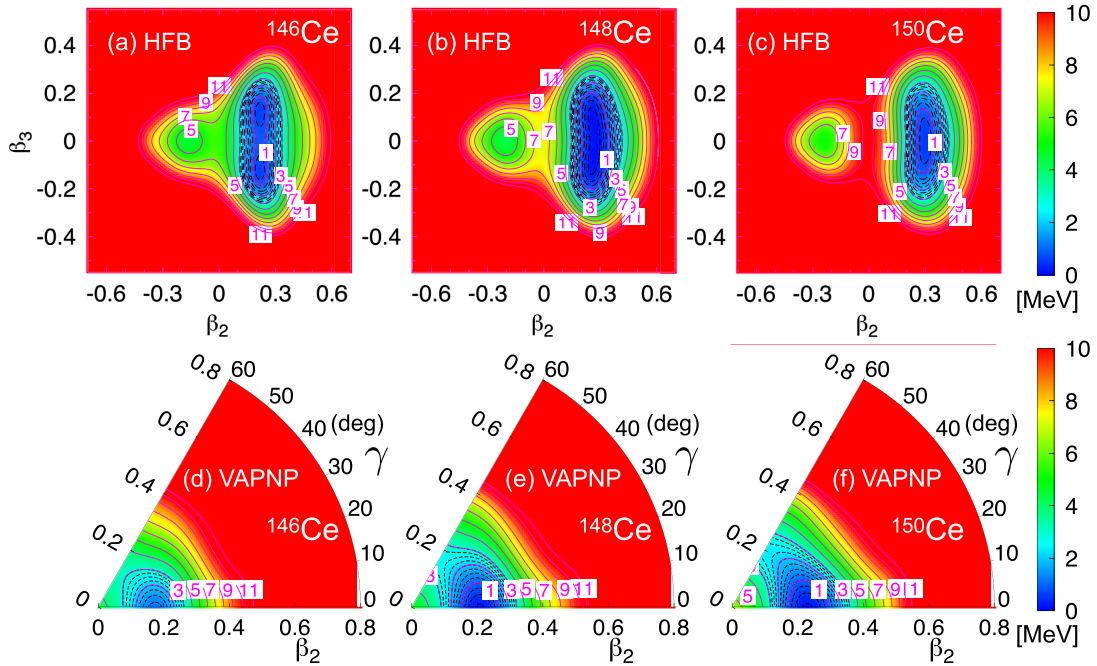


FIG. 8. (a)–(c) HFB energy surfaces along the axial  $\beta_2$ - $\beta_3$  plane and (d)–(f) VAPNP energy surfaces along the triaxial  $\beta_2$ - $\gamma$  plane computed for the  $^{146-150}\text{Ce}$  isotopes with the Gogny D1S interaction.

is also present in the positive-parity states. The negative-parity band is built on top of the same quadrupole deformation as the positive-parity one and peaks at a non-zero value of  $\beta_3$ . The  $\text{SCCM}_{(\beta_2,\gamma)}$  results can only predict positive parity states. In

this case, apart from the axial prolate ground-state bands ( $0_1^+$ ,  $2_1^+$ ,  $4_1^+$ , etc.), other bands built on top of prolate  $0_2^+$ , triaxial  $2^+$ , and triaxial  $4^+$  states are found that can be associated to  $\beta$  bands, (mostly)  $K = 2$  ( $\gamma$  bands) and (mostly)  $K = 4$  bands,

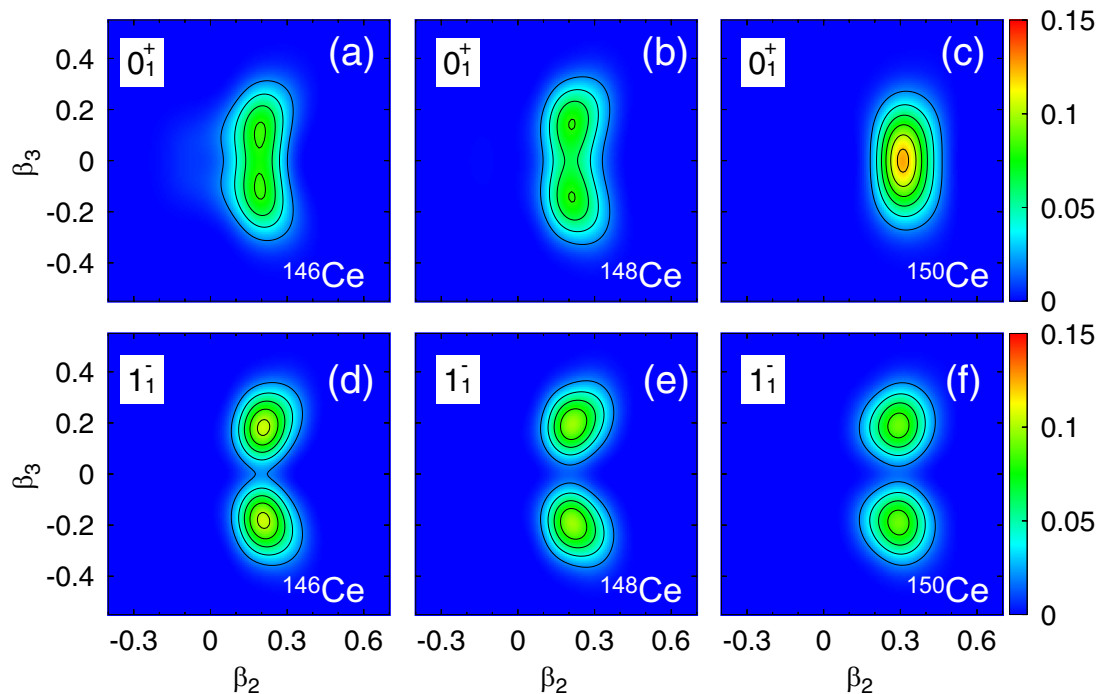


FIG. 9. (a)–(c) Ground-state and (d)–(f)  $1_1^-$  collective wave functions in the  $\beta_2$ - $\beta_3$  plane obtained with the  $\text{SCCM}_{(\beta_2,\beta_3)}$  method for the  $^{146-150}\text{Ce}$  isotopes.



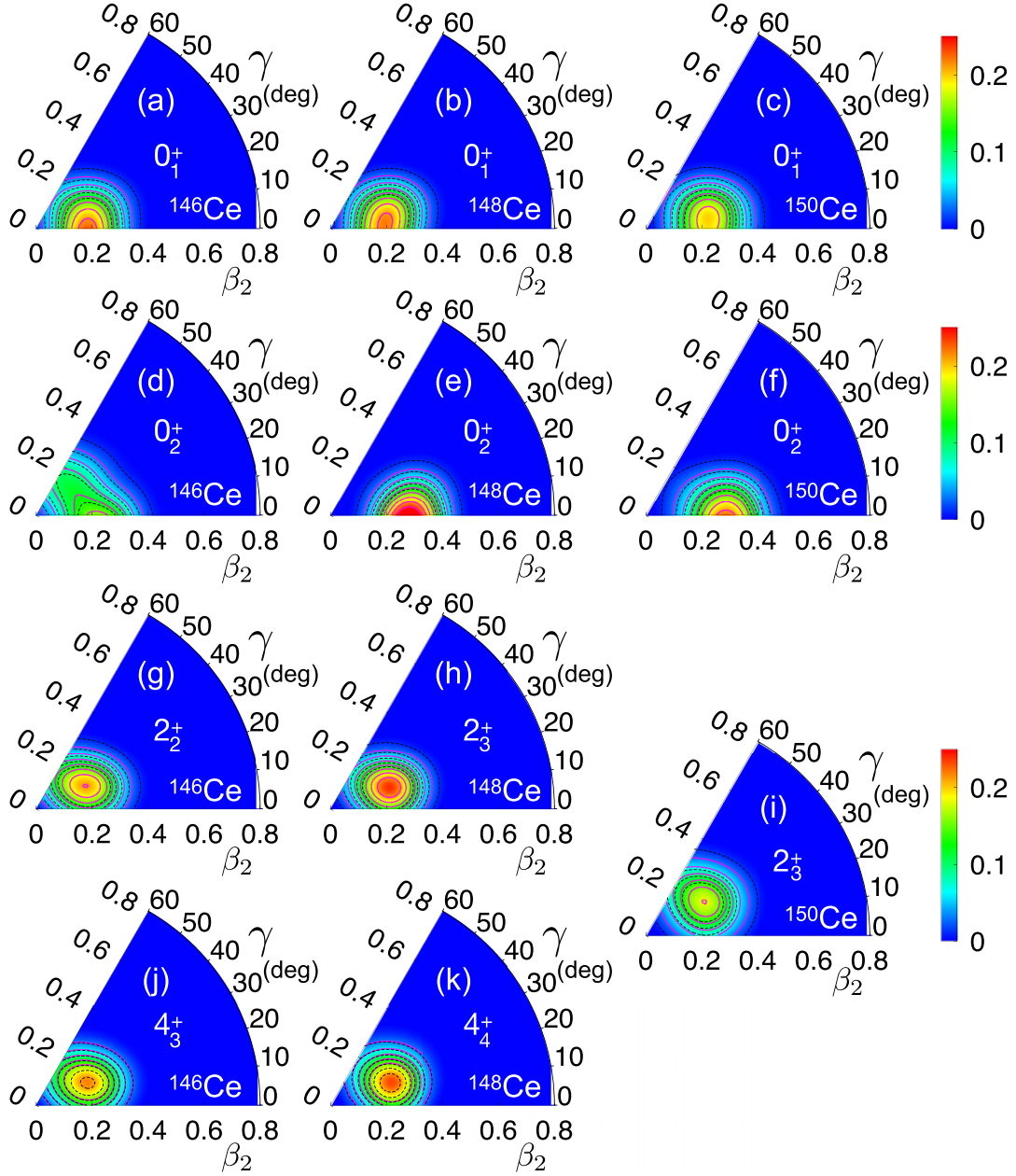


FIG. 10. (a)–(k) Collective wave functions in the  $\beta_2$ - $\gamma$  plane for the band heads obtained with the  $\text{SCCM}_{(\beta_2, \gamma)}$  method for the  $^{146-150}\text{Ce}$  isotopes.

respectively. In Fig. 10 the c.w.f.'s for those band heads are plotted.

We finally discuss the ability of the above SCCM methods to reproduce the experimental data. In Table I we show the predicted  $2_1^+$ ,  $4_1^+$ ,  $1_1^-$ , and  $3_1^-$  excitation energies, the reduced transition probabilities  $B(E2, 2_1^+ \rightarrow 0_1^+)$  and  $B(E2, 4_1^+ \rightarrow 2_1^+)$ , and the corresponding available experimental results. We see that both SCCM approaches reproduce nicely the experimental trends although the excitation energies, especially for the positive parity states, are systematically overestimated. This is a well-known effect of this kind of calculations and is related to the lack of time-reversal symmetry breaking

(cranking) states in the set of HFB-like wave functions that are mixed within the GCM method. The SCCM is a variational method and, in the present implementations, the ground state energy is privileged with respect to the excited state energies. As a consequence, the spectrum is stretched. This stretching is state-dependent, i.e., it could affect differently to the  $2_1^+$  and  $2^+$   $\gamma$  states, for example. This deficiency can be corrected by adding the cranking states [41,42], but it is very time consuming [43] and we expect that the qualitative description of the nuclei under study will not change significantly. We also observe in the  $B(E2)$  values that the deformation of the nucleus  $^{146}\text{Ce}$  ( $^{148}\text{Ce}$  is overestimated (underestimated) in

TABLE I. Experimental and SCCM excitation energies (in MeV) and  $B(E2)$  reduced transition probabilities (in W.u.) for the lowest states in  $^{146-150}\text{Ce}$  isotopes.

$2_1^+$	Exp	SCCM $_{(\beta_2, \beta_3)}$	SCCM $_{(\beta_2, \gamma)}$		
146	0.258	0.304	0.352		
148	0.158	0.216	0.291		
150	0.097	0.118	0.258		
$4_1^+$	Exp	SCCM $_{(\beta_2, \beta_3)}$	SCCM $_{(\beta_2, \gamma)}$		
146	0.668	0.742	1.038		
148	0.453	0.640	0.890		
150	0.305	0.389	0.767		
$2_1^+ \rightarrow 0_1^+$	Exp	SCCM $_{(\beta_2, \beta_3)}$	SCCM $_{(\beta_2, \gamma)}$		
146	43	55	53		
148	85	74	59		
$4_1^+ \rightarrow 2_1^+$	Exp	SCCM $_{(\beta_2, \beta_3)}$	SCCM $_{(\beta_2, \gamma)}$		
146	–	92	80		
148	130	112	89		
	$1_1^-$ (exp)	$1_1^-$ SCCM $_{(\beta_2, \beta_3)}$	$3_1^-$ (exp)	$3_1^-$ SCCM $_{(\beta_2, \beta_3)}$	
146	0.925	0.670	0.961	0.911	
148	(0.453)	0.506	(0.841)	0.761	
150	–	0.863	–	1.074	

both SCCM approaches, although the method that includes both quadrupole and octupole degrees of freedom provides better results.

Anyhow, the qualitative structure of the nucleus should be reasonably well-described within the present SCCM, i.e., for  $^{148}\text{Ce}$  we find a prolate rotational ground state band with a triaxial  $K = 2$   $\gamma$  band, a triaxial  $K = 4$  band related to it, and a second prolate  $0^+$  excited state band (slightly more deformed than the g.s. band). Unfortunately, in the present status without cranking, we cannot say much about the  $X(5)$  nature of this nucleus.

## VII. CONCLUSIONS

We analyzed five experimental fingerprints of the  $X(5)$  phase transition point based on different energy ratios, namely  $R_{42} = E(4_1^+)/E(2_1^+)$ ,  $R_{022} = E(0_2^+)/E(2_1^+)$ ,  $R_{222} = E(2_{2,\beta}^+)/E(2_1^+)$ ,  $R_{60} = E(6_1^+)/E(0_2^+)$ , and  $R_{422} = E(4_2^+)/E(2_2^+)$ . We found that the first four ratios are close to the  $X(5)$  limit values for  $N = 90$  ( $^{148}\text{Ce}$ ), but the modest increase of the fingerprints for cerium isotopes around  $N = 90$  indicates that the  $X(5)$  limit is less pronounced than for other  $X(5)$  nuclei,  $^{150}\text{Nd}$ ,  $^{152}\text{Sm}$ , and  $^{154}\text{Gd}$ .

In spite of the fact that we cannot reproduce a first order phase transition such as  $X(5)$  within the ACM, we can fit the model parameters to experimental energies of transitional nuclei, such as  $^{146}\text{Ce}$  and  $^{148}\text{Ce}$ . Moreover, contrary to the  $X(5)$  limit, the position of the lowest  $2^+$   $\gamma$  band is well defined by the model parameters of the ACM. The ACM calculations of  $^{146}\text{Ce}$  and  $^{148}\text{Ce}$  confirm  $^{148}\text{Ce}$  as a better candidate for an  $X(5)$  nucleus based on its ground-state band properties, but, simultaneously, one observes a lot of characteristics that depart from the  $X(5)$  limit for excited bands in this nucleus.

Both microscopic approaches based on the Skyrme and Gogny forces predict prolate ground-state deformation and shallow octupole deformation for  $^{146}\text{Ce}$  and  $^{148}\text{Ce}$  that tends to disappear for  $^{150}\text{Ce}$ . Moreover, the SCCM calculations indicate triaxiality in excited positive-parity bands for nonzero spins. There are no clear signatures of an  $X(5)$  limit in the microscopic calculations. Instead, quite flat potential energy surfaces in  $\beta_3$  around the prolate  $\beta_2$  minimum are observed, thus resembling a phase transition critical point that could be approximated by an infinite square well in  $\beta_3$ . Therefore, from the theoretical point of view it would be interesting to focus in future investigations on a possible extension of the  $X(5)$  model to take into account also octupole degrees of freedom with an infinite square well in both  $\beta_2$  and  $\beta_3$  to find possible spectral signatures of an axial phase transition from  $U(5)$  to  $SU(3)$  via a quadrupole-octupole soft system.

From the experimental point of view, future investigations should focus on measurements of inter- and intraband transitions in excited bands, in particular on  $B(E1)$  and  $B(E3)$  transition probabilities between negative-parity band(s) and the ground-state band to check the predicted octupole deformation or softness.

## ACKNOWLEDGMENTS

This work was supported by Projects No. SP2021/64 and No. SP2022/25 financed by the Czech Ministry of Education, Youth and Sports. M.A. acknowledges also the financial support from Project No. CZ.02.1.01/0.0/0.0/16 013/0001791, IT4 Innovations National Supercomputing Center - Path to Exascale, and G.T. acknowledges the financial support of the Czech Academy of Sciences and the French-Czech LEA NuAG collaboration. T.R.R. acknowledges the financial support of the Spanish MICINN under PGC2018-094583-B-I00 and the computer resources provided by GSI-Darmstadt and Centro de Computación Científica-Universidad Autónoma de Madrid (CCC-UAM) computing facilities.

- [1] F. Iachello, *Phys. Rev. Lett.* **87**, 052502 (2001).  
 [2] R. Bijker, R. F. Casten, N. V. Zamfir, and E. A. McCutchan, *Phys. Rev. C* **68**, 064304 (2003).  
 [3] D. Bonatsos, D. Lenis, N. Minkov, P. P. Raychev, and P. A. Terziev, *Phys. Rev. C* **69**, 014302 (2004).  
 [4] D. Bonatsos, E. A. McCutchan, N. Minkov, R. F. Casten, P. Yotov, D. Lenis, D. Petrellis, and I. Yigitoglu, *Phys. Rev. C* **76**, 064312 (2007).

- [5] R. F. Casten, *Prog. Part. Nucl. Phys.* **62**, 183 (2009).  
 [6] R. F. Casten and N. V. Zamfir, *Phys. Rev. Lett.* **87**, 052503 (2001).  
 [7] R. Krücken, B. Albanna, C. Bialik, R. F. Casten, J. R. Cooper, A. Dewald *et al.*, *Phys. Rev. Lett.* **88**, 232501 (2002).  
 [8] R. M. Clark, M. Cromaz, M. A. Deleplanque, M. Descovich, R. M. Diamond, P. Fallon *et al.*, *Phys. Rev. C* **68**, 037301 (2003).

- [9] N. Pietralla and O. M. Gorbachenko, *Phys. Rev. C* **70**, 011304(R) (2004).
- [10] D. Tonev, A. Dewald, T. Klug, P. Petkov, J. Jolie, A. Fitzler *et al.*, *Phys. Rev. C* **69**, 034334 (2004).
- [11] J. Wiederhold, R. Kern, C. Lizarazo, N. Pietralla, V. Werner, R. V. Jolos *et al.*, *Phys. Rev. C* **94**, 044302 (2016).
- [12] Z. P. Li, T. Niksic, D. Vretenar, J. Meng, G. A. Lalazissis, and P. Ring, *Phys. Rev. C* **79**, 054301 (2009).
- [13] Z. P. Li, T. Niksic, D. Vretenar, and J. Meng, *Phys. Rev. C* **81**, 034316 (2010).
- [14] P. Koseoglou, V. Werner, N. Pietralla, S. Ilieva, T. Niksic, D. Vretenar *et al.*, *Phys. Rev. C* **101**, 014303 (2020).
- [15] P. Koseoglou, Lifetime measurements in the neutron rich  $^{148}\text{Ce}$  nuclide at the low-Z boundary of the  $N = 90$  shape-phase transition, Ph.D. thesis, TU Darmstadt, 2019.
- [16] Z. P. Li *et al.*, *J. Phys. G: Nucl. Part. Phys.* **43**, 024005 (2016).
- [17] P. Klüpfel, J. Erler, P.-G. Reinhard, and J. A. Maruhn, *Eur. Phys. J. A* **37**, 343 (2008).
- [18] T. R. Rodríguez and J. L. Egido, *Phys. Rev. C* **81**, 064323 (2010).
- [19] D. Bonatsos, E. A. McCutchan, R. F. Casten, and R. J. Casperson, *Phys. Rev. Lett.* **100**, 142501 (2008).
- [20] A. Bohr and B. R. Mottelson, *Nuclear Structure II*, 1st ed. (Benjamin, New York, 1974).
- [21] P. O. Hess, J. A. Maruhn, and W. Greiner, *J. Phys. G: Nucl. Phys.* **7**, 737 (1981).
- [22] G. Gneuss and W. Greiner, *Nucl. Phys. A* **171**, 449 (1971).
- [23] D. J. Rowe, T. A. Welsh, and M. A. Caprio, *Phys. Rev. C* **79**, 054304 (2009).
- [24] D. J. Rowe, *Nucl. Phys. A* **735**, 372 (2004).
- [25] D. J. Rowe and P. S. Turner, *Nucl. Phys. A* **753**, 94 (2005).
- [26] M. A. Caprio, *Phys. Rev. C* **72**, 054323 (2005).
- [27] T. A. Welsh and D. J. Rowe, *Comput. Phys. Commun.* **200**, 220 (2016).
- [28] D. J. Rowe and J. L. Wood, *Fundamentals of Nuclear Models: Foundational Models* (World Scientific, Singapore, 2010), Vol. 2.
- [29] D. J. Rowe, *Phys. Rev. Lett.* **93**, 122502 (2004).
- [30] D. J. Rowe, *Nucl. Phys. A* **745**, 47 (2004).
- [31] M. Abolghasem *et al.*, *Phys. Scr.* **95**, 034010 (2020).
- [32] [www.nndc.bnl.gov/ensdf](http://www.nndc.bnl.gov/ensdf).
- [33] M. Bender, P.-H. Heenen, and P.-G. Reinhard, *Rev. Mod. Phys.* **75**, 121 (2003).
- [34] P. Klüpfel, P.-G. Reinhard, T. J. Bürvenich, and J. A. Maruhn, *Phys. Rev. C* **79**, 034310 (2009).
- [35] W. J. Huang, G. Audi, M. Wang, F. G. Kondev, S. Naimi, and X. Xu, *Chin. Phys. C* **41**, 030002 (2017).
- [36] J. Terasaki, P.-H. Heenen, H. Flocard, and P. Bonche, *Nucl. Phys. A* **600**, 371 (1996).
- [37] J. A. Maruhn, P.-G. Reinhard, P. D. Stevenson, and A. S. Umar, *Comput. Phys. Commun.* **185**, 2195 (2014).
- [38] R. Fossion, D. Bonatsos, and G. A. Lalazissis, *Phys. Rev. C* **73**, 044310 (2006).
- [39] R. N. Bernard, L. M. Robledo, and T. R. Rodríguez, *Phys. Rev. C* **93**, 061302(R) (2016).
- [40] L. M. Robledo, T. R. Rodríguez, and R. R. Rodríguez-Guzmán, *J. Phys. G: Nucl. Part. Phys.* **46**, 013001 (2019).
- [41] M. Borrajo, T. R. Rodríguez, and J. L. Egido, *Phys. Lett. B* **746**, 341 (2015).
- [42] J. L. Egido, M. Borrajo, and T. R. Rodríguez, *Phys. Rev. Lett.* **116**, 052502 (2016).
- [43] T. R. Rodríguez, *Eur. Phys. J. A* **52**, 190 (2016).